Evaluation of a 3D local multiresolution algorithm for the correction of partial volume effects in positron emission tomography.

Adrien Le Pogam, Mathieu Hatt, Patrice Descourt, Nicolas Boussion,
Charalampos Tsoumpas, Federico E. Turkheimer, Caroline Prunier-Aesch,
Jean-Louis Baulieu, Denis Guilloteau, Dimitris Visvikis

Evaluation of a 3D local multiresolution algorithm for the correction of partial volume effects in positron emission tomography

Adrien Le Pogam [1] , Mathieu Hatt [2] [*] , Patrice Descourt [2] , Nicolas Boussion [2] , Charalampos Tsoumpas [4] , Federico E. Turkheimer [1] , Caroline Prunier-Aesch [2] , Jean-Louis Baulieu [3] , Denis Guilloteau [2] , Dimitris Visvikis [2]

[1] *PET Methodology Hammersmith Hospital Campus, Du Cane Road , Clinical Sciences Centre (MRC) , Imperial College London , W12 0NN London,GB*

[2] *LATIM, Laboratoire de Traitement de l'Information Medicale INSERM : U650 , Université de Bretagne Occidentale - Brest , Institut Télécom , Télécom Bretagne , CHU Brest , Université européenne de Bretagne , Hopital Morvan, 5 Avenue Foch, 29609 Brest Cedex,FR*

[3] *Imagerie et cerveau INSERM : U930 , Université François Rabelais - Tours , CNRS : ERL3106 , Hôpital Bretonneau, 1 Bd Tonnelle 37044 Tours,FR*

[4] *Division of Imaging Sciences King's College , St. Thomas' Hospital, westminster Bridge Road, London, UK*

* Correspondence should be adressed to: Mathieu Hatt <hatt@univ-brest.fr >

Abstract
Purpose

Partial volume effects (PVE) are consequences of the limited spatial resolution in emission tomography leading to under-estimation of uptake in tissues of size similar to the point spread function (PSF) of the scanner as well as activity spillover between adjacent structures. Among PVE correction methodologies, a voxel-wise mutual multi-resolution analysis (MMA) was recently introduced. MMA is based on the extraction and transformation of high resolution details from an anatomical image (MR/CT) and their subsequent incorporation into a low resolution PET image using wavelet decompositions. Although this method allows creating PVE corrected images, it is based on a 2D global correlation model which may introduce artefacts in regions where no significant correlation exists between anatomical and functional details.

Methods

A new model was designed to overcome these two issues (2D only and global correlation) using a 3D wavelet decomposition process combined with a local analysis. The algorithm was evaluated on synthetic, simulated and patient images, and its performance was compared to the original approach as well as the geometric transfer matrix (GTM) method.

Results

Quantitative performance was similar to the 2D global model and GTM in correlated cases. In cases where mismatches between anatomical and functional information were present the new model outperformed the 2D global approach, avoiding artefacts and significantly improving quality of the corrected images and their quantitative accuracy.

Conclusions

A new 3D local model was proposed for a voxel-wise PVE correction based on the original mutual multi-resolution analysis approach. Its evaluation demonstrated an improved and more robust qualitative and quantitative accuracy compared to the original MMA methodology, particularly in the absence of full correlation between anatomical and functional information.

MESH Keywords Algorithms ; Artifacts ; Brain ; radionuclide imaging ; Humans ; Imaging, Three-Dimensional ; methods ; Linear Models ; Positron-Emission Tomography ; methods ; Reproducibility of Results ; Whole Body Imaging

Author Keywords emission tomography ; partial volume effects ; resolution and intensity recovery ; wavelet transform ; multi-modality

INTRODUCTION

Partial volume effects (PVE) refers to two distinct phenomena leading in under- or over-estimation of the tissues uptake. The first results from the limited spatial resolution of the imaging device, leading to a 3-dimensional (3D) blurring and a loss of signal in tissues of size similar to the system's point spread function (PSF) Full Width at Half Maximum (FWHM), as well as activity cross-contamination (" spillover") between structures with different uptakes[1]. The second phenomenon arises from the discrete representation on a grid with voxel sizes from 1 to 5 mm for the reconstruction of images. The voxel values at the edges are consequently a mixture of different tissues, an effect commonly known as "tissue fraction effect". This effect exists on all image modalities but its magnitude is lower on anatomical datasets such as MRI or CT, and the introduction of higher resolution details from anatomical images in the functional images could reduce its impact. In this study we considered both the spatial resolution of the scanner and the voxel grid sampling, which are specific to the low resolution images obtained with PET.

Most of the previously proposed approaches for PVE correction consist in using *a priori* anatomical information provided by either computed tomography (CT) or magnetic resonance (MR) images. Although these methodologies usually aim at the recovery of accurate uptakes in specific regions of interest (ROIs)[1 ̂4] requiring either a co-registered atlas or a segmentation step, such as the ROI based geometric transfer matrix (GTM) by Rousset et al[2], some voxel-based implementations have been recently proposed. They could be classified in two groups; namely deconvolution without the use of anatomical information[5 ̂8] or voxel-wise correction based on the use of anatomical and functional images available from multi-modality devices[9 ̂11].

Teo *et al.* [5] considered the use of iterative deconvolution restricted to a ROI to avoid noise increase in the overall image, while a more recent study applied iterative deconvolution to brain images[6]. Boussion *et al.* [7] proposed the use of wavelet-based denoising at the iterative level of the deconvolution process to avoid noise amplification. The efficacy of this denoising greatly depends on the choice of the wavelet filtering algorithm and associated threshold values. Kirov *et al.* [8] suggested the use of regularized iterative deconvolution with variance control based on local topology as an alternative solution for noise reduction. This latter approach is not fully automatic because the determination and optimisation of the regularization parameters are dependent on the properties of the image.

One methodology based on the use of anatomical information to correct functional data was proposed by Boussion *et al.* [9] and is referred to as mutual multi-resolution analysis (MMA). It uses discrete wavelet transforms[10] of a low resolution PET image L and a corresponding co-registered high resolution anatomical MRI (or CT) image H. The method extracts the spatial frequencies like details, edges, and textures from wavelet decompositions at a level of resolution common to H and L (a specific decomposition layer in which both wavelet images have the same PSF FWHM). A global linear model is then inferred to build the lacking details of L from these found in H. The method demonstrated accurate quantitative correction comparable with the methodologies considered as the current state of the art[2 ̂ 4] but limited to ROI analyses. This approach has the advantage of generating PVE corrected images, allowing for an accurate activity recovery, without any segmentation or other pre-processing steps.

Despite these advantages, the original MMA approach suffers from two limitations. First, it is based on a global correlation between anatomical and functional structures, as a linear and global link is assumed in order to model the relation between the wavelet coefficients of both modality transforms at the same level of resolution. Consequently, where there is little to no correlation between these structures, artifacts may appear in the corrected emission image as a result of the incorporation of anatomical structures with no functional significance. An alternative approach based on MMA has been recently published[11] restricted to the brain domain and making use of atlases for the provision of the anatomical information in an attempt to reduce the impact of functional and anatomical image mismatches. However such approach is dependent on the use of atlases and is therefore only applicable to brain imaging. The second limitation of the original MMA algorithm is due to the use of a 2D modeling as the correction is applied independently slice by slice, whereas PVE is a 3D effect for which it is important to consider interactions in all three spatial directions.

The goal of the present study was to design a new model in order to overcome the shortcomings associated with the original MMA algorithm as highlighted above. More specifically, a new 3D wavelet decomposition scheme was designed and the global linear relation model was replaced with an improved local analysis, in order to process limited image areas at a time and adapt this model to each image part based on local information. This new approach was evaluated on synthetic and simulated images, and applied to brain and whole body patient datasets, and its performance was compared to the results obtained with both the original 2D global MMA algorithm described by Boussion *et al.* [9] and the GTM reference methodology[2].

MATERIALS AND METHODS

Multiresolution analysis in the wavelet domain

Performing multiresolution image analysis using wavelet transforms consists in analyzing details across different levels of resolution or scale[12], in order to extract consecutive layers of details from large structures to small edges, by separating the spatial frequencies they contain. Among the many algorithms developed to perform wavelet transform of an image, the most common approach is the multi-resolution pyramidal methodology[13] consisting in iteratively reducing the resolution of the image. Such sub-sampling may cause a loss of linear continuity in spatial features such as edges and the appearance of artifacts in those structures[14]. Therefore, the undecimated algorithms are often more appropriate, for instance for the image fusion purpose[15]. The "à trous" ("with holes") algorithm was used here and extended to 3D to perform the wavelet decomposition[10] based on the initial work of Boussion *et al.* [9]. This algorithm presents several advantages such as a straightforward implementation, a reconstruction without any loss of information and an isotropic process (i.e. no specific directions selected). This algorithm is related to the standard discrete wavelet transform decomposition scheme[16] as it performs the sub-sampling of the filtered image by up-sampling the low-pass filter; inserting zeros between each of the filter's coefficient at each level. The detail coefficients images $\{w_j\}$ are then obtained as the difference $\{I_{j+1} - I_j\}$ between the low-pass filtered images from two consecutive levels. At each iteration j, the resolution of the image I_j is reduced to obtain the smoothed image I_{j+1} (called residual) using:

$$I_{j+1}(x, y, z) = \sum_{m,n,o \in [-2,2]} h(m, n, o) I_j(x + m \cdot 2^j, y + n \cdot 2^j, z + o \cdot 2^j)$$

(1)

where h is a 3D low-pass filter defined by:

$$h(x, y, z) = h_{1D}(x) {}^* h_{1D}(y) {}^* h_{1D}(z)$$
$$h_{1D}(0) = 3/8, h_{1D}(\pm 1) = 1/4\ h_{1D}(\pm 2) = 1/16, \text{ and } h_{1D}(n) = 0 \text{ if } |n| > 2$$

(2)

with * the convolution operator and h_{1D} a binomial filter[17] of order 4.

The inverse transform can be computed by adding the detail layers $\{w_j\}$ from all levels to the final low-resolution image I_J:

$$I_0(x, y, z) = I_J(x, y, z) + \sum_{j=1}^{j=J} w_j(x, y, z)$$

(3)

where, J is the number of iterations from the initial image I_0 to the final approximation I_J.

Due to the discrete convolution shown in equation 1, the spatial resolution (or PSF FWHM) of the residual image I_{j+1} depends on both the spatial resolution of I_j and the size of its voxels. This is because the image I_j is sampled according to the iteration index j (i.e. the level of scale in the wavelet transform) and the convolution leads to a non linear dependency (factor 2^j) on the resulting PSF FWHM of the residual I_{j+1}. The relationship between voxel sizes and the residual FWHM at different scales was determined by applying the "à trous" algorithm to an initial point source of different sizes (from 0.6 to 1.4 mm) using the Mathematica software. This relationship was found to be linear (see table 1). In order to change the voxel size of the initial image I_0 and to obtain a residual I_j with a specific spatial resolution according to the Mathematica software analysis, trilinear interpolation and 3rd order B-spline resampling were used for anatomical and functional images respectively.

Using both equation 3 and this resampling, the spatial frequencies $\{w_j\}$ of the anatomical and functional images are extracted in 3D and the spatial resolution of the final residual I_J is accurately determined. We define the spatial resolution of the anatomical image H as q, (initial image H referred to as H_q) and that of the functional image L as r = q + p, (initial image L referred to as L_r), with r>q and p the number of decompositions that have to be performed to reach a common level of resolution between the two modalities. This number is deduced from the PSF FWHM and the voxel sizes of both initial images. We can then perform the extraction of the spatial frequencies at a level of resolution common to H and L (q+p+1), using the "à trous" algorithm:

$$L_r(x, y, z) = L_{q+p}(x, y, z) = L_{q+p+1}(x, y, z) + w_{q+p+1}^L(x, y, z)$$

(4)

$$H_q(x, y, z) = H_{q+p+1}(x, y, z) + \sum_{k=1}^{k=p+1} w_{q+k}^H(x, y, z)$$

(5)

where, W^L and W^H are the wavelet coefficients from the wavelet decomposition of the functional and anatomical images respectively.

Local mutual multiresolution analysis

Similarly to previously developed methodologies using wavelets for PVE correction[9,11], our method is based on the exploitation of existing correlations in the wavelet domain. Such correlation is defined by establishing a relationship between the anatomical and functional wavelet coefficients at a common level of resolution, independently of the original images content (in terms of units). In our proposed approach, we assume that the residual L_r can be estimated by a space dependent scaling of H_r, for which the scaling factor can be obtained from a local analysis to account for local differences between H and L. The corrected emission image Lq (same level of resolution as Hq) is therefore obtained using equation 6 by adding the original uncorrected value of L ($L_{q+p+1}(x, y, z) + w_{q+p+1}^L(x, y, z)$, see eq. 4) with the sum of the anatomical wavelet coefficients weighted by a local factor α:

$$L_q(x, y, z) = L_{q+p+1}(x, y, z) + w_{q+p+1}^L(x, y, z) + \alpha(x, y, z) \sum_{k=1}^{k=p} w_{q+k}^H(x, y, z)$$

(6)

where α stands for the Median of the Ratio Map (MRM). Equation 6 provides the corrected value for each voxel (x, y, z) by adding to the original functional image value (L) the wavelet coefficient. Each voxel is processed individually however the parameter α is computed for each voxel using a 3D sliding cube, simultaneously applied within the L and H wavelet layers to obtain the MRM (eq.7).

$$\alpha(x, y, z) = \text{median}\left\{\frac{W_{q+p+1}^{L}(x_i, y_i, z_i)}{T(W_{q+p+1}^{H}(x_i, y_i, z_i))}, (x_i, y_i, z_i) \in WIND\right\}$$

(7)

where WIND is a window in 3D (i.e. a cube) centered on (x,y,z) with a fixed size of 3×3×3 voxels (i=1...3) and T is a threshold operator. Equation 7 therefore computes α for each voxel of coordinates x, y, z, as the median (within a cube centered on this voxel) of the ratios between the wavelets coefficients of each transforms. The cubic moving window was introduced instead of a simple voxel–by–voxel ratio to account for local variations in the anatomical and functional images, contrary to the global model[9] and to reduce the noise and mis-registration sensitivity associated with a voxel–by–voxel analysis. The choice of using the median instead of the mean within the cubic sliding window, as well as the actual size of the cube was made based on the results obtained on simulations (see results section). Different sizes (3, 5 and 7 voxels) were compared since this parameter might have an impact on the sensitivity of the method to spatial mis-registration, noise and inappropriate choice of the respective PSF FWHM values. Also, results obtained using the mean or the median of the ratios were compared. The mean was expected to be more sensitive to artefacts and noise in contrast to the median, which would tend to discard extreme values. Also, the use of a sliding cube should also make the approach more robust to spatial mis-registration or inaccurate PSF FWHM values used in the process. On the one hand, the ratio map allows a large amount of uncorrelated details such as anatomical structures without significant uptake in the functional image to be discarded. On the other hand, if no structural information is associated with a significant uptake in the corresponding functional image, the low values of the wavelet coefficients may lead to MRM evaluation errors with denominator values W_{q+p+1}^{H} close to zero. In order to avoid extreme values that may be generated by the MRM and preserve the activity of the functional image in such configurations, we introduced a fixed threshold T (equation 7) on the anatomical wavelet coefficients. Its value was empirically chosen as 0.1 as it gave satisfactory results in most considered cases, however future studies should investigate the automatic estimation of an optimal value for each case. Therefore an investigation regarding the cube optimal size was carried out in this study.

Validation and comparison study

Analysis

Mean and associated standard deviation were computed on ROI placed on the organs or objects of interest in order to quantify the partial volume effect correction, and compared to the ground-truth when available (synthetic images and simulated datasets). In such cases (for example the spheres), the ROI were defined on the ground-truth, covering the entire structure voxel-by-boxel, and were reported to both uncorrected and corrected images. For clinical datasets, as ground-truth was not available, the improvement between uncorrected and corrected image was reported for ROI placed on both images.

Synthetic images

The proposed algorithm was first validated using synthetic images. All the images considered in this section were generated in 3D and analyzed either on a 2D basis using the original MMA method, or in 3D using the proposed approach. Finally, the GTM methodology was also applied, assuming a perfect knowledge of the ground-truth for the definition of the necessary ROIs in order to eliminate any potential errors that can be associated with a segmentation step. Two different synthetic images were employed, the first one H_{ref} (figure 1-(1)) to generate the functional images L (figure 1-(2)), and the second one H_{anat} (figure 1-(3)) used for the correction of PVE via both the 2D global and 3D local methodologies. A Gaussian noise (standard deviation (SD) 2% of the mean in the uniform part of the phantom) was added in the H_{anat} images prior to their use for the correction. These 128×128×128 (1×1×1 mm³ voxels) images contain a cylindrical background region with a fixed intensity of 100 and spheres of different sizes and intensities. The first (figure 1-(A)-(1)) contains five 2cm diameter spheres with decreasing intensities (200, 120, 90, 70 and 50). The second one (figure 1-(B)-(1)) contains four spheres of decreasing diameter (6, 4, 2 and 1 cm) with intensity of 200. The last two images (figure 1-(C)-(1) and 1-(C)-(3)) display spheres common to both modalities with however no absolute intensity correlation, as well as two additional structures: one which is present only in the anatomical data H_{anat} with no corresponding uptake in the functional image and respectively a hot spot in the functional data L without any corresponding anatomical structure in H_{anat}.

The L images (figure 1-(2)) (same voxel size and dimensions as for H_{anat}) were generated by convolving H_{ref} (figure 1-(1)) with a 6 mm FWHM 3D Gaussian PSF and adding Gaussian noise (SD 10% of the mean intensity). In this first dataset, both H_{anat} and L images had a voxel size of 1mm³. The Gaussian noise approximation is realistic enough for the reconstructed PET images when considering a specific ROI[18]. The noise intensity (SD value) used was determined through different ROI analysis in the lung and liver from various whole body clinical datasets.

Different combinations of the 3D synthetic images in figure 1 were considered to compare the performance of the different approaches considered. First, functional and anatomical images with complete structural and intensity correlation (figure 1-(A)-(2) and figure 1-(A)-(3)) were used to specifically study the accuracy of the correction for spillover effects due to the various contrasts. A second combination was analyzed (figure 1-(B)-(2) and figure 1-(B)-(3)) in order to examine the value recovery of small objects. These two

configurations were designed to validate the performance of the local approach for cases where the global approach already leads to satisfactory results, i.e. with a perfect match (structure and intensity) between both modalities. A third combination was used to investigate partial correlation between the two modalities (figure 1-(C) (2) and (3)) for which the 2D global MMA is expected to perform with reduced qualitative and quantitative accuracy. In each case, the new local 3D MMA approach was compared to the previous 2D global model and to the GTM method.

Finally, tests similar to those already used for the 2D MMA[9] were carried out to evaluate the impact of noise and possible mis-registration errors, or an inappropriate choice of FWHM parameters. For this purpose, variable noise intensities (SD from 10 to 50%) were added to the functional images of figure 1-(C)-(2) . The robustness of the approach against mis-registration errors was evaluated by applying different rigid transformations (translation up to 4 voxels (about 4mm), rotation up to 5°) or inappropriate scaling (±10%) to the functional image of figure 1-(C)-(2) . The impact of an inappropriate choice of FWHM parameters for the resampling was investigated by generating different L images from the H_{ref} (figure 1-(C)-(1)) with FWHM PSF from 4 to 8 mm. These L images were then corrected for PVE considering a unique FWHM value of 6 mm.

Simulated images

In the second part of this study, simulated images generated using a segmented brain phantom based on measured T1 MRI images[19] were analyzed. The images are a T1-weighted MRI and an associated [18] F-FDG PET. The functional image was generated using the following procedure[20]. Clinically measured plasma time activity curves (TACs) were first used to generate a set of TACs for each anatomical region of the brain phantom according to 28 different clinical dynamic frames (1×30sec, 1×15sec, 1×5sec, 4×10sec, 4×30sec, 4 ×60sec, 4×120sec, 9×300sec). Pathological parameters were introduced in the parietal and the anterior frontal lobes. The dynamic images were then forward-projected using the maximum ring difference, mash and span as for the patient study, forming projection data of the ECAT HR+ scanner (spatial resolution of 4.8mm and 5.6mm FWHM transaxially and axially respectively). These projection data were attenuated using the values of the different tissue types contained in the Zubal phantom (muscle, bone, fat, skin), and uncorrected for normalization by applying the inverse normalization factors. These factors and the scatter additive term were both taken from the human study. The randoms contribution was simulated based on the system's detection efficiency factors pattern scaled to the total random events of each frame in the acquired human study. Finally, Poisson noise was added to the sinograms and the images were finally reconstructed with filtered backprojection including scatter, attenuation and normalization corrections. The image sizes for both PET and MRI were 128 ×128×64 (2.35×2.35×2.42 mm^3 voxels). The final static PET image was eventually obtained by summing the last six temporal frames. The respective considered FWHM were 4.8 mm in plane and 5.6 mm axially for the PET images and 1 mm in all three dimensions for the anatomical datasets. The performance of the method was assessed by comparison with the known ground-truth of the simulation. This dataset was also used to determine the optimal sliding cube size among 3×3×3, 5×5×5 or 7×7×7 voxels (see results section).

Clinical images

The approaches were also compared on two clinical images. The first one consists of a clinical T1 MRI (GE 1.5T) and associated FDG brain PET (Philips GEMINI dual slice PET/CT) scans. The MRI images were chosen instead of the CT for the correction to benefit from the improved contrast in the different brain structures. The MRI image contains a hyper-intensity signal in the left occipital lobe and the posterior cingulum due to the gadolinium injection. The PET reconstructed images (using RAMLA 3D (2 iterations, relaxation parameter of 0.05 and a 5mm FWHM 3D Gaussian post-filtering) and CT based attenuation correction) are 128×128×64 (1.41×1.41×2mm^3 voxels) and the MRI is 512×512×160 (0.47×0.47×1mm^3 voxels). The PET and MRI images were spatially co-registered using mutual information maximization and affine transformations using MIPAV software (Center for Information Technology (CIT National Institutes of Health (NIH)). The FWHM considered was 1mm and 5mm in all three dimensions for the MRI and PET datasets respectively (considering the spatial resolution for the Philips GEMINI PET system of 5.2mm and 5.4mm FWHM transaxially and axially respectively in combination with the 5mm FWHM Gaussian post-filtering applied to the reconstructed image). Qualitative evaluation was carried out using profiles through the frontal and the tempo-occipital regions. Quantitative accuracy was evaluated by white and grey matter quantification (mean intensity and standard deviation) before and after PVE correction using an automatic delineation on the MRI image via the voxel-based morphometry segmentation tool of the SPM software[21]. The same delineation results were used for the ROI based correction using GTM for comparison. The impact of the 3D analysis was observed on this dataset in which voxels are anisotropic.

The second dataset is a whole-body [18] F-FDG-PET/CT image of a lung cancer patient (GE Discovery STE 4-slice PET/CT), acquired 55 minutes after injection of 355 MBq (CT: 80mA, 140kVp, PET: 3mins per axial field of view). PET images were reconstructed (voxel size of 4.68×4.68×3.27mm^3 and a matrix size of 128×128×47 voxels) using OSEM (2 iterations, 28 subsets) and CT based attenuation correction. The resolution of the original CT image was 0.97×0.97×0.97mm^3 voxels (matrix dimension 421×321×100). The FWHM of the PET image was considered as 6.1mm and 6.7mm in plane and axially respectively (matching the spatial resolution of GE Discovery STE), and 1 mm in all three directions for the CT images. Manually drawn spherical regions were placed on the lesion (ROI$_{lesion}$) and in the lung (ROI$_{normal}$). An additional ROI in the spinal region (ROI$_{bone}$) was used in order to evaluate the potential of introducing artefacts in the PVE corrected PET images as a result of prominent anatomical structures (such as bones) in the CT images which are not present in the

FDG PET images. Since no ground-truth is available in this case, anatomical images were semi-automatically segmented to generate ROIs for the tumor, the lungs, soft tissues and bones in order to be used in the GTM method.

RESULTS

Synthetic images

The quantitative results regarding the correction using the three methods can be found in figure 1 (D-F) for the three different synthetic datasets. Figure 1-(D) contains results of the spillover effects correction for the spheres of constant size and varying intensities (fig. 1-(A)). It displays the percentage of recovered intensity (a value of 100 is a perfect recovery of the true activity) in the spheres, demonstrating similar levels of recovery for the three methods, within 2% for all of the different intensities considered. Figure 1-(E) shows quantification results for the constant intensity and variable size spheres (figure 1-(B)). The recovered intensities in the spheres demonstrate that both approaches perform with similar accuracy. As the functional image is resampled with the voxel size of the anatomical image as a first step for both methodologies, the impact of tissue-fraction effect is reduced by introducing the higher resolution details of the anatomic imaging when available and correlated, achieving accurate intensity recovery even for the smallest spheres where PVE have the most significant impact. Figures 1-(C)-(4) and -(5) show the results for the uncorrelated case in which the spheres are different in the functional and anatomical images in terms of both intensity and structure, revealing differences between the 2D global and new 3D local approaches as the new approach does not incorporate uncorrelated anatomical details in the functional image during the correction, whereas the 2D global MMA creates local artifacts related to existing mismatches. In addition, the local approach handles more accurately the differences in absolute signal intensity between the anatomical and functional images. A quantitative comparison of recovered intensities in the spheres is shown in figure 1-(F) and demonstrates much higher accuracy for the new approach: without correction, the mean error was −11.4% ± 5.2% whereas the 2D global and 3D local corrections resulted in a mean error of −15.1% ± 6.1% and 2.8% ± 2.4% respectively. The GTM method resulted in a mean error of 3.2%. The standard deviation of each measurement associated with the use of the 2D global MAA approach was much larger than when applying the new model. This is explained by the artifacts that are introduced due to mismatch in structural information between anatomical and functional datasets that the 2D global approach is not able to address. Such a case highlights the limitation of the 2D global MMA and the way the new 3D approach successfully overcomes such issues, with similar accuracy to GTM using the ground-truth ROIs. The measurements in sphere 7 illustrate the fact that no PVE correction can be performed due to the lack of corresponding structure in the anatomical image. It is important however to emphasize that in such a case, the functional activity in the corrected image remains unchanged and no additional artifact is introduced.

The local approach appeared more robust with respect to the increase of noise in the functional image in figure 1(C)-(2)): mean recovered intensity across all structures (excluding sphere 7) and the different noise levels was 99.5 ± 1.1% for the 3D local whereas the 2D global results exhibited much higher standard deviation with a mean recovery intensity of 97.8 ± 27.8% as illustrated in figure 2-(A) .

The impact of an inappropriate choice of FWHM value and of a spatial misalignment between the anatomical and functional images was investigated for the 3D local MMA only as such an analysis has already been performed by Boussion *et al.* [1] for the 2D global approach only. This analysis demonstrated overall satisfactory robustness with however recovery errors reaching 25 to 50% for certain spheres although the spatial misalignments and rotations considered were smaller (up to 3mm and 3° respectively). For the present study of the 3D local MMA robustness, a maximum mean error of 1.9% ± 23.1% was reached with the investigated misalignment, rotations and inadequate scaling parameters (figure 2-(B)). Regarding the inadequate choice of FHWM parameters, the mean error was 9.4 ± 5.5% and 2.8 ± 3% for ± 2mm and ± 1mm around the actual exact value (figure 2-(C)).

Simulated images

Figures 3-(B) and (C) illustrate the correction obtained using the mean and the median of the ratios respectively (use to establish the factor α), on the simulated ^{18}F-FDG brain PET and associated T1-weighted MRI images of fig. 3-(A) . The impact of the cube size (3×3× 3, 5×5×5 and 7×7×7 voxels in (1), (2) and (3) respectively) is also illustrated. Irrespectively of the cube size, the mean of the ratio led to major artifacts due to noise and the possible approximations in the FWHM parameters. On the contrary, the use of the median led to better visual result. Only small visual differences (mostly a slight increasing blurring effect) were observed with the three different cube sizes (figure 3-(C)-(1) to 3-(C)-(3)). This blurring effect can be explained by the inclusion of additional voxels for the computation of the median value and a less efficient local modeling. The quantitative analysis as shown in figure 3-(D) demonstrated higher activity recovery when using the smallest cubic window size (3×3×3). All other results were therefore generated with this setting.

Figure 4-(A) shows the results obtained on the simulated ^{18}F-FDG brain PET images. The global 2D MMA led to the incorporation of all the MRI details into the corrected PET images (figure 4-(A)-(3)), creating artifacts such as uptake corresponding to the skull, whereas the image corrected with the new approach (figure 4-(A)-(4)) was free of such artifacts. Further evaluation using a frontal region profile is presented in figure 4-(B) , demonstrating higher contrast with the local approach. Both grey and white matters are better delineated. The spikes on both sides of the profile (see red arrows in figures 4-(A)-(3) and 4-(B)), corresponding to the artifact uptake from the bone incorporation using the global MMA approach, are absent from the corrected image using the new model. Comparison of ROI values

placed in different regions of the brain against the true image (figure 4-(C) (1–5)) demonstrated higher accuracy of the correction with the new approach. In some regions such as amygdala, cerebellum or thalamus, the 2D global MMA and the GTM approach accurately corrected the intensities. However, in other regions such as the frontal or the hippocampus region for instance, it led to an over- or under-estimation of the uptake respectively. Mean error for all analyzed regions was 31.9 ± 8.5%, 21.3 ± 6.8%, 16.7% ± 5.7% and 8.9 ± 2.7 % for the non corrected PET, 2D global MMA, GTM and 3D local MMA respectively.

Clinical images

As a last evaluation step the new approach was applied and compared to the global MMA and GTM on two clinical cases: a brain and a whole-body acquisition (fig. 5 and 6 respectively). Despite the good correlation between the T1 MRI (fig. 5-(A)-(1)) and FDG PET (fig. 5-(A)-(2)) images regarding the grey and white matter, non-correlated structures also exist, such as the skull (see red arrows) and the gadolinium enhancement (see white circle) in the MRI image. These MRI features, which do not match any FDG uptake, were introduced in the corrected image by the 2D global process (fig. 5-(A)-(3)), whereas the 3D local approach (fig. 5-(A)-(4)) suppressed these uncorrelated details, leading to a more reliable and visually satisfying PVE correction. In addition, the new approach led to higher contrast between regions as shown in the profiles of figure 5-(B) . Furthermore, using the SPM software to segment the grey and white matter from the MRI images, we obtained quantitative results for the comparison of the two voxel-wise correction methodologies as well as corrected values using the GTM approach in these ROIs. The 2D global MMA led to higher standard deviation values due to the incorporation of additional uncorrelated details, with an average mean intensity variation with respect to the initial PET image in the grey and white matter regions of 1.8 ± 21.1% and 0.2 ± 31.6% respectively. In contrast, higher mean intensity variations and lower standard deviation were obtained with the new approach: 11.4% ± 6.5% in the grey matter and −2.6% ± 8.3% in the white matter. The new approach therefore led to less noisy and higher uptake enhancements than the 2D global MMA. By comparison, the use of GTM led to +10% and −19% mean activity changes for the grey and white matter ROIs respectively.

The whole-body [18] F-FDG PET/CT image (fig. 6-(1) and 6-(2)) of a patient with lung cancer was analyzed in order to assess the potential of our new approach regarding oncology applications. Figure 6 contains the correction results using both approaches, demonstrating the incorporation of artifacts such as the spine with the global approach (fig. 6-(3)) whereas the new model allowed avoiding them fig. 6-(4)). Quantitative measurements in this bone region demonstrated an uptake increase of 28.8 ± 25.4% with the 2D global whereas the 3D local led to a much lower variation (1.9 ± 11.3%). Table 2 contains the results of quantitative analysis using ROIs placed in the tumor and the lung, revealing an increase in lesion-to-lung ratio of 33.5% with the global approach, 45.8% with the GTM method and 54.1% with the 3D local approach. Furthermore, a variation in the whole lung activity concentration of 13.3% with the global approach was measured, whereas the new model leads to a smaller variation of only 6.7% thanks to the fact that it disregards anatomical structures in the lungs without matching FDG uptake. A similar variation of 5.4% of the lung uptake was obtained with the GTM approach.

DISCUSSION

Multi-modality PET/CT imaging is rapidly becoming the gold standard for diagnostic studies especially in oncology with [18] F-FDG PET/CT. PET/CT systems are now widely used in clinical practice thanks to the automatic fusion of functional and anatomical information they provide. Accurate and efficient PVC in this context might demonstrate significant clinical impact for instance for the detection of small lesions in whole-body PET acquisitions, or for the assessment of therapy response during or after treatment. In addition, new technology developments now allow the simultaneous acquisition of PET and MRI images for clinical brain studies[22] and it is expected this will be also extended to whole-body imaging. These developments facilitate the use of anatomical information either during the reconstruction (attenuation correction[23 ,24] or incorporation of a-priori information[25 ,26]) or as a post-processing step for the improvement of qualitative and quantitative accuracy of functional images (denoising[27] or partial volume correction[9 ,11]).

The recently introduced MMA methodology for partial volume correction[9] is based on the mutual multi-resolution analysis of a functional image and the corresponding anatomical one. In contrast to the standard PVE correction approaches using anatomical information[2], the MMA is voxel-wise and hence does not use ROIs obtained from a segmentation of the anatomical images. The algorithm was validated on synthetic and simulated datasets with accuracy similar to the reference GTM approach with the advantage of not requiring an atlas or a segmentation step as well as leading to PVE corrected images which are subsequently available for further analysis. There was however certain limitations associated with its 2D implementation and the use of a strictly linear and global model. This model results in the incorporation of every anatomical detail into the functional image and can therefore lead to artifacts in the corrected images where no correlation exists between anatomical and functional details. For example, the methodology has been shown to work well with a combination of FDG PET and T1 MRI brain images[9 ,28], but its performance with respect to receptor brain PET imaging has not been demonstrated.

In this study, we have developed and evaluated a new model for MMA, based on a locally adaptive 3D analysis in order to address the limitations of the 2D global MMA previous implementation. An accurate co-registration is considered as a pre-requisite to both MMA and

our new proposed approach, although we also demonstrated satisfactory robustness of the method to mis-registration errors. The implementation is based on the extension of the 2D analysis to the 3D and the introduction of a local model. The impact of each of the two modifications has not been evaluated individually. On the one hand, the 3D analysis provides a better representation of the PSF convolution which is a 3D phenomenon, allowing an accurate wavelet decomposition of the image compared to the 2D approach. The local analysis applied to this 3D decomposition allows computing a more accurate model which is subsequently used for the correction, compared to the simple global approach.

In addition, in order to discard uncorrelated details, the initial linear model coefficient was replaced by a new one based on the median value (rather than the mean) of the voxel-by-voxel ratios in a local cube centered on each voxel. Consequently, the 3D anatomical details in the wavelet domain are discarded in the regions where there is no matching functional uptake. The validation of the new model was performed on synthetic and simulated datasets. The results demonstrated similar quantitative performance with the 2D global approach and the GTM in the case of correlated datasets (figures 1-(A), 1-(B)). It is worth noting that the GTM was applied using the available ground-truth for the definition of the ROIs, leading this way to the best possible results with this approach. In addition, the performance was significantly improved for non-correlated structural and functional image combinations (figures 1-(C) , figure 4). The new model was also evaluated using clinical whole-body and brain datasets. For both these clinical datasets we obtained a significantly improved image quality without artefacts, as well as higher contrast improvements, compared to the 2D global MMA correction (figures 5 –6). However in the absence of ground-truth, the absolute accuracy of the recovered activity values and spatial spread of the structures of interest (such as small tumors) could not be directly assessed on these datasets.

Although this new approach allows improved qualitative and quantitative voxel-wise partial volume correction using anatomical information, without assuming homogeneous uptake in regions of interest as the GTM approach, and is applicable to both brain and oncology imaging, one should consider potential pitfalls associated with any postprocessing PVE correction approach based on anatomical information. As the correction is performed based on the anatomical image details, if no or not enough information is available for a specific structure, the PVE correction will be either not possible or incomplete. The new proposed approach is certainly able to handle mismatches between anatomical and functional information. However, in the case of tumour imaging, if the lesion is necrotic in the functional image but there is no corresponding necrosis in the anatomical structure, the correction will be incomplete as only the external outline of the lesion will be corrected. Absence of contrast in the anatomical dataset corresponding to a specific structure would lead to a lack of significant wavelet coefficients in the wavelet decomposition of such a structure, therefore no correction can be deduced and applied to the corresponding functional uptake. However, when a relationship exists between the anatomical signal and the functional one, such an issue may be overcome by using alternative acquisition protocols in order to generate such contrast. For instance, a contrast enhanced anatomical imaging or different sequences available in MRI imaging will be certainly interesting in enhancing the potential of PVC approaches such as our own for newly developed PET/MRI devices. Finally, one can identify the areas of the image where no significant PVE correction was applied as a result of lack of anatomical details by analyzing the MRM. This map indeed contains the correction that was applied to each voxel and very low or zero values correspond to little or no correction. It is also important to emphasize that the tissue fraction effect can be corrected only where the frontier between tissues can be extracted from anatomical images. This effect can in addition only be reduced, not entirely corrected, as it also exists in the anatomical datasets, although with a lower magnitude than in the functional images.

Another potential limitation of voxel-wise partial volume correction approaches based on the use of anatomical images may come from the dependency of the algorithm on the noise level in both the anatomical and functional images. However, our approach demonstrated high robustness versus noise. In addition, the local aspect of the correlation model greatly reduces the sensitivity of the correction to potential artefacts/distortions present in the anatomical images.

Mis-registration is also a limiting factor for multimodality PVE correction approaches such as the one reported in this work. However, current techniques[29 ̄31] allow fully automated 3D elastic image registration and can accurately align (with errors within 1 to 2 voxels) whole-body PET and CT images acquired on standalone as well as on combined PET-CT scanners. Furthermore, although both the 2D and 3D approaches are sensitive to a spatial registration error between the anatomical and functional images, the different tests carried out on synthetic images with translation movements up to 4 voxels and rotation movements up to 5°, as well as inappropriate scaling of the anatomical image showed limited impact with a maximum error of 1.9% ± 23.1% thanks to the use of the sliding cube and the median of the ratios. However misregistration should be limited to a minimum in order to ensure the most accurate correction, since large translations and rotations might lead to errors up to 25%.

Finally, as with any post-processing PVE correction algorithm the new model requires the exact knowledge of both modalities' spatial resolution (FHWM) and voxel sizes in order to determine the parameters of the wavelet decomposition scheme. However, our new methodology also demonstrated satisfactory robustness versus errors up to 2mm in the choice of the FWHM parameters. After images co-registration, the process is automatic and takes from about a minute to several minutes (depending on the size of the images) on a desktop computer.

We assumed a constant value of the PSF FWHM in the entire image, which is a simplification considering the potential variation of the PSF FWHM throughout the field of view, especially in the case of whole body imaging. This aspect could be improved by modeling the exact PSF FWHM in each direction according to the spatial position of the analyzed voxel. Finally, an automatic estimation of the threshold T value regarding the wavelets coefficients might improve the results on a case by case basis. Future studies will also investigate the performance of post-reconstruction processing approaches such as the one developed in this study with the incorporation of the PSF and other *a priori* information into the reconstruction iterative algorithm. Within this context a couple of existing studies have shown similar performance between the post-processing deconvolution and PSF incorporated reconstruction based PVE correction approaches [[32 ,33]], with the generic advantage of post-reconstruction approaches being reconstruction algorithm independent.

CONCLUSION

We developed an improved voxel-wise methodology to correct for partial volume effects in emission tomography. This new model overcomes limitations encountered in the originally proposed MMA and allows for a more universal approach that can potentially handle any combination of co-registered anatomical and functional images. Our new methodology extends the 2D MMA to a 3D local analysis, in which local details are conditionally taken into account in the correction process. PVE correction was successfully applied to images with either high correlation, for which the 2D MMA correction was already adequate, or more challenging cases for which correlation between anatomical and functional datasets was not complete and for which global 2D MMA failed by introducing artefacts and led to inaccurate quantification. The local 3D process was successfully tested and validated on synthetic, simulated and clinical datasets, with similar performance to the reference GTM method without requiring a segmentation step, producing PVE corrected images, and avoiding artifacts generated by the 2D global approach. In addition it proves to be overall more robust with good accuracy and robustness without particular requirements regarding the structural and intensity correlations between the anatomical and functional images.

References:

- 1 . Aston JA , Cunningham VJ , Asselin MC , Hammers A , Evans AC , Gunn RN . Positron emission tomography partial volume correction: estimation and algorithms . J Cereb Blood Flow Metab . 22 : 1019 - 1034 2002 ;
- 2 . Rousset OG , Ma Y , Evans AC . Correction for partial volume effects in PET: principle and validation . J Nucl Med . 39 : 904 - 911 1998 ;
- 3 . Meltzer CC , Kinahan PE , Greer PJ , Nichols TE , Comtat C , Cantwell MN , Lin MP , Price JC . Comparative evaluation of MR-based partial-volume correction schemes for PET . J Nucl Med . 40 : 2053 - 2065 1999 ;
- 4 . Rousset OG , Collins DL , Rahmim A , Wong DF . Design and implementation of an automated partial volume correction in PET: application to dopamine receptor quantification in the normal human striatum . J Nucl Med . 49 : 1097 - 1106 2008 ;
- 5 . Teo BK , Seo Y , Bacharach SL , Carrasquillo JA , Libutti SK , Shukla H , Hasegawa BH , Hawkins RA , Franc BL . Partial-volume correction in PET: validation of an iterative postreconstruction method with phantom and patient data . J Nucl Med . 48 : 802 - 810 2007 ;
- 6 . Tohka J , Reilhac A . Deconvolution-based partial volume correction in Raclopride-PET and Monte Carlo comparison to MR-based method . Neuroimage . 39 : 1570 - 1584 2008 ;
- 7 . Boussion N , Cheze Le Rest C , Hatt M , Visvikis D . Incorporation of wavelet-based denoising in iterative deconvolution for partial volume correction in whole-body PET imaging . Eur J Nucl Med Mol Imaging . 36 : 1064 - 1075 2009 ;
- 8 . Kirov AS , Piao JZ , Schmidtlein CR . Partial volume effect correction in PET using regularized iterative deconvolution with variance control based on local topology . Phys Med Biol . 53 : 2577 - 2591 2008 ;
- 9 . Boussion N , Hatt M , Lamare F , Bizais Y , Turzo A , Cheze-Le Rest C , Visvikis D . A multiresolution image based approach for correction of partial volume effects in emission tomography . Phys Med Biol . 51 : 1857 - 1876 2006 ;
- 10 . Dutilleux P . An implementation of the "algorithme a trous" to compute the wavelet transform . Time-Frequency Methods and Phase Space . 1 : Springer-Verlag ; Marseille, France 1987 ; 298 - 304
- 11 . Shidahara M , Tsoumpas C , Hammers A , Boussion N , Visvikis D , Suhara T , Kanno I , Turkheimer FE . Functional and structural synergy for resolution recovery and partial volume correction in brain PET . Neuroimage . 44 : 340 - 348 2009 ;
- 12 . Daubechies I . The wavelet transform, time-frequency localization and signal analysis . IEEE Trans Inf Theory . 36 : 961 - 1005 1990 ;
- 13 . Mallat S . A theory for multiresolution signal decomposition: the wavelet representation . IEEE Trans Pattern Anal Mach Intell . 11 : 674 - 93 1989 ;
- 14 . Yocky DA . Artifacts in wavelet image merging . Opt Eng . 53 : 2094 - 2101 1995 ;
- 15 . Amolins Krista . Wavelet based image fusion techniques - An introduction, review and comparison . ISPRS Journal of Photogrammetry & Remote Sensing . 62 : 249 - 263 2007 ;
- 16 . Shensa MJ . The discrete wavelet transform: wedding the a trous and Mallat algorithms . IEEE Trans Inform Theory . 40 : 2464 - 2482 1992 ;
- 17 . Starck JL , Fadili J , Murtagh F . The undecimated wavelet decomposition and its reconstruction . IEEE Trans Image Process . 16 : 297 - 309 2007 ;
- 18 . Hatt M , Cheze le Rest C , Turzo A , Roux C , Visvikis D . A fuzzy locally adaptive Bayesian segmentation approach for volume determination in PET . IEEE Trans Med Imaging . 28 : 881 - 893 2009 ;
- 19 . Zubal IG , Harrell CR , Smith EO , Rattner Z , Gindi G , Hoffer PB . Computerized three-dimensional segmented human anatomy . Med Phys . 21 : 299 - 302 1994 ;
- 20 . Tsoumpas C , Turkheimer FE , Thielemans K . Study of direct and indirect parametric estimation methods of linear models in dynamic positron emission tomography . Med Phys . 35 : 1299 - 1309 2008 ;
- 21 . Ashburner J , Friston KJ . Voxel-based morphometry--the methods . Neuroimage . 11 : 805 - 821 2000 ;
- 22 . Schlemmer HP , Pichler BJ , Schmand M , Burbar Z , Michel C , Ladebeck R , Jattke K , Townsend D , Nahmias C , Jacob PK , Heiss WD , Claussen CD . Simultaneous MR/PET imaging of the human brain: feasibility study . Radiology . 248 : 1028 - 1035 2008 ;
- 23 . Kinahan PE , Townsend DW , Beyer T , Sashin D . Attenuation correction for a combined 3D PET/CT scanner . Med Phys . 24 : 2046 - 2053 1998 ;
- 24 . Visvikis D , Costa DC , Croasdale I , Lonn AH , Bomanji J , Gacinovic S , Ell PJ . CT-based attenuation correction in the calculation of semi-quantitative indices of [18F] FDG uptake in PET . Eur J Nucl Med Mol Imaging . 30 : 344 - 353 2003 ;
- 25 . Comtat C , Kinahan PE , Fessler JA , Beyer T , Townsend DW , Defrise M , Michel C . Clinically feasible reconstruction of 3D whole-body PET/CT data using blurred anatomical labels . Phys Med Biol . 47 : 1 - 20 2002 ;
- 26 . Nuyts J , Baete K , Beque D , Dupont P . Comparison between MAP and postprocessed ML for image reconstruction in emission tomography when anatomical knowledge is available . IEEE Trans Med Imaging . 24 : 667 - 675 2005 ;
- 27 . Turkheimer FE , Boussion N , Anderson AN , Pavese N , Piccini P , Visvikis D . PET image denoising using a synergistic multiresolution analysis of structural (MRI/CT) and functional datasets . J Nucl Med . 49 : 657 - 666 2008 ;

- 28 . Boussion N , Cheze-Le Rest C , Bizais Y , Visvikis D . Quantitative assessment by means of realistic simulated images and patient data of a new method for partial volume correction effects in brain PET . Journal of Nucl Med . 192P - 2006 ;
- 29 . Shekhar R , Walimbe V , Raja S , Zagrodsky V , Kanvinde M , Wu G , Bybel B . Automated 3-dimensional elastic registration of whole-body PET and CT from separate or combined scanners . J Nucl Med . 46 : 1488 - 1496 2005 ;
- 30 . Sorzano CO , Thevenaz P , Unser M . Elastic registration of biological images using vector-spline regularization . IEEE Trans Biomed Eng . 52 : 652 - 663 2005 ;
- 31 . Frost & Sullivan . Emerging *Technology Developments in Fusion Technology for Diagnostic Imaging* . Technical Insights . 2005 ;
- 32 . Le Pogam A , Alessio AM , Kandel B , Kirov AS , Barrett O , Fernandez P , Cheze Le Rest C , Visvikis D . Comparison of PET reconstruction resolution recovery and post-reconstruction deconvolution for PET partial volume correction . J Nucl Med . 51 : S2 - 577 - 2010 ;
- 33 . Hoetjes NJ , van Velden FH , Hoekstra OS , Hoestra CJ , Krak NC , Lammertsma AA , Boellaard R . Partial volume correction strategies for quantitative FDG PET in oncology . Eur J Nucl Med Mol Imaging . 37 : 1679 - 1687 2010 ;

Figure 1

Three synthetic datasets for which the background region has a fixed value of 100. (A) a correlated case with spheres of constant size and decreasing intensities (from 200 to 50), (B) a correlated case with spheres of constant intensity (200) and decreasing sizes, and (C) an uncorrelated case. For each one of the three synthetic datasets: (1) a high-resolution anatomical image H_{ref} used to generate the low-resolution functional image L (2), (3) the high-resolution anatomical image H_{anat} used for the PVE correction, (4) the PVE corrected images using the 2D global approach and (5) images after PVE correction using the 3D local approach. Percentage of intensity recovery (mean ± SD) for the three datasets corrected for PVE using the GTM (mean only), 2D global or 3D local approach: (D) a correlated case with spheres of constant size and decreasing intensities, (E) a correlated case with spheres of constant intensity and decreasing sizes, and (F) an uncorrelated case. Spheres are numbered on figure 1-(1).
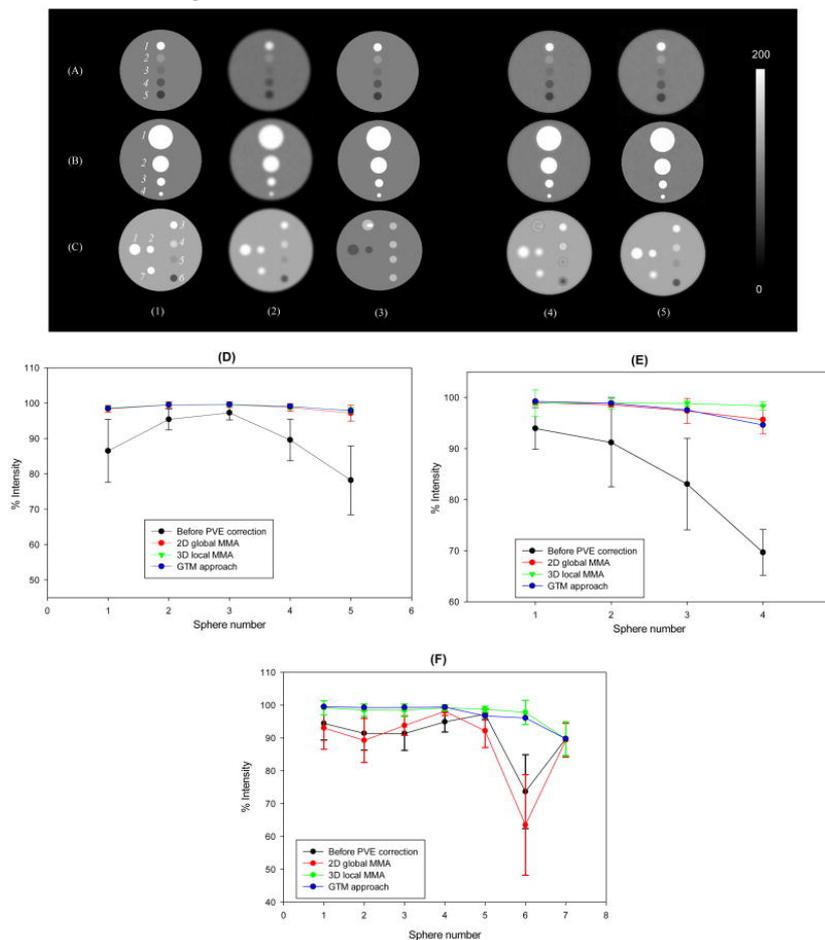
Figure 2

(A) Percentage of mean recovered intensity relative to true values (mean ± SD) across all structures of figure 1-(C)-(1) (excluding sphere 7) and the different noise levels (SD from 10 to 50%) in figure 1-(C)-(2) . Percentage error of recovered intensity relative to true values (mean ± SD) in the different spheres (figure 1-(C)-(1)) considering: (B) different spatial misalignment scenarios between figures 1-(C)-(2) and 1-(C)-(3) (translation up to 4 voxels, rotation up to 5°) or inappropriate scaling (±10%) of figure 1-(C)-(2) ; (C) different PSF sizes (4mm to 8mm) in the PVE correction process relative to the true value (6mm).
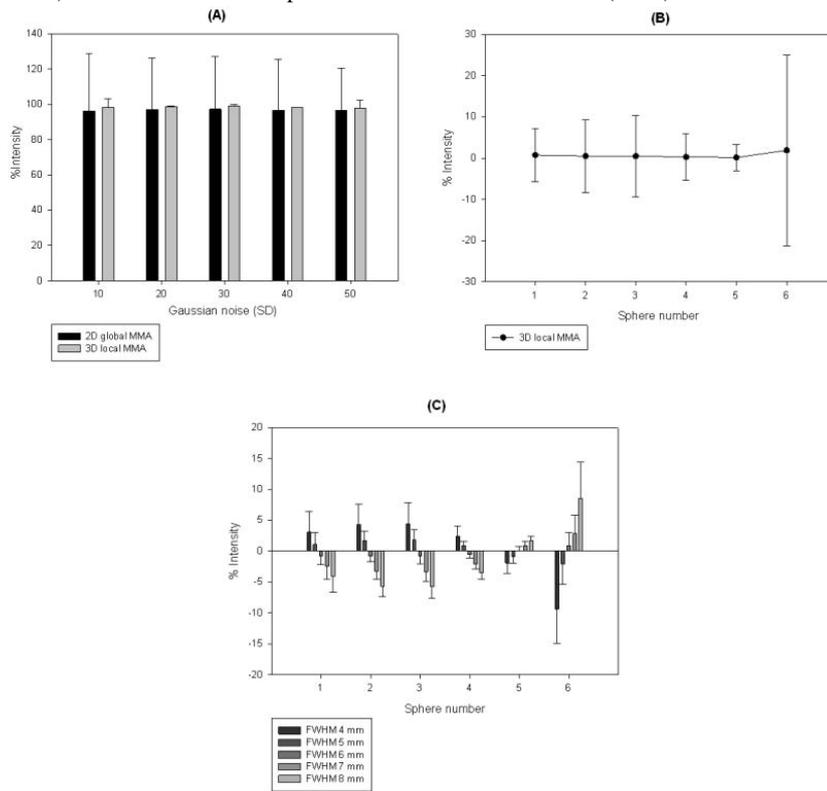
Figure 3

Optimization and validation for the local modeling parameters on (A) a simulated FDG PET (A)-(2)/MRI (A)-(3) brain dataset (ground truth on figure (A)-(1)) using (B) the mean and (C) the median of the ratio maps methodologies for respectively a (1) 3×3×3, (2) 5×5×5 and (3) 7×7 ×7 3D cube. (D) % intensity recovery in the different brain structures considered in the simulation following the PVE correction.
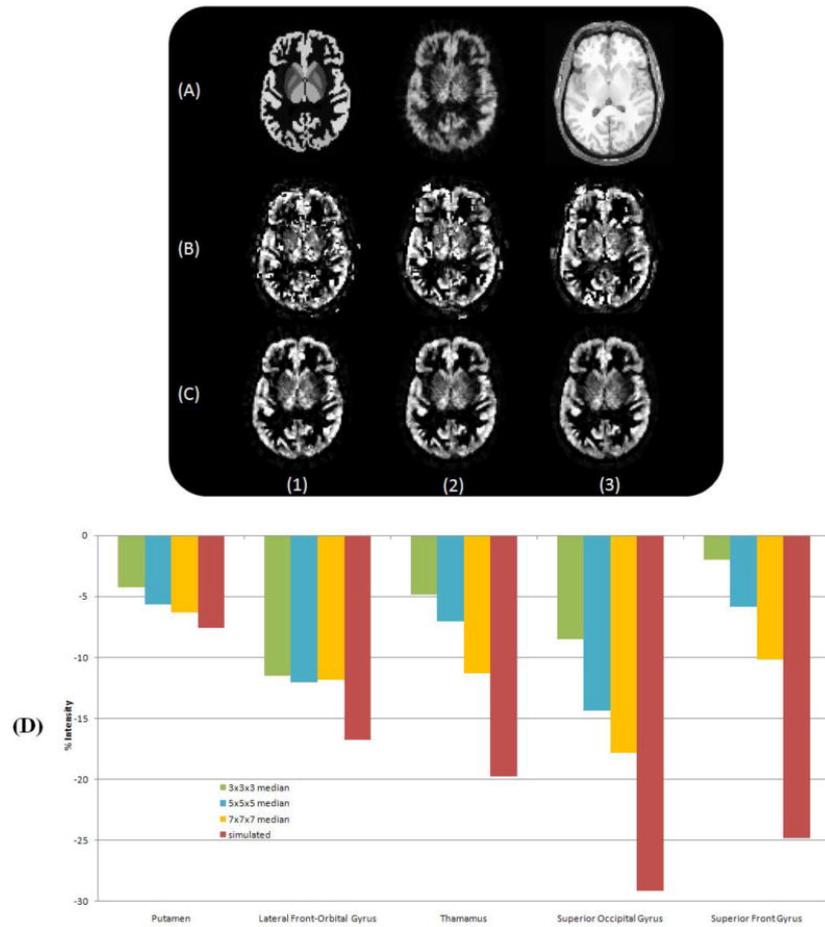

Figure 4

(A) PET images of the simulated brain ^{18}F-FDG PET/T1-weighted MRI dataset: (1) T1-weighted MRI, (2) non-corrected PET, (3) 2D global, and (4) 3D local MMA based PVE corrected images. (B) Profile results across the frontal cortex on the uncorrected and PVE corrected PET images. (C) ROI quantification intensity (mean value ± SD) comparisons between measured (black solid lines) and true image values (magenta dotted lines): (1) for the simulated image, and recovered from the corrected images using the (2) 2D global, (3) 3D local MMA and (4) GTM approach. The ROIs and the associated true activity concentration values used in the simulation are shown in C-(5) based on the segmented T1-weighted MRI image (showing highlighted a frontal region of interest).
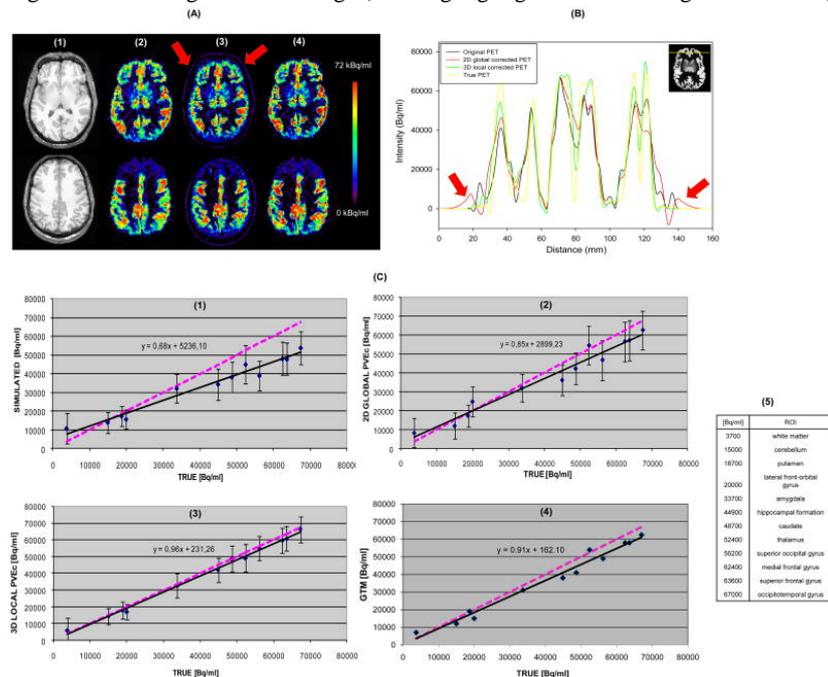
Figure 5

(A) a clinical brain T1-weighted MRI/[18] F-FDG PET with injection of gadolinium contrast: (1) T1-weighted MRI, (2) non-corrected [18] F-FDG PET image, (3) 2D global, and (3) 3D local MMA based PVE corrected images. (B) Profile results across the frontal and occipital cortex regions on the uncorrected and PVE corrected PET brain images corresponding to the datasets shown in (A).
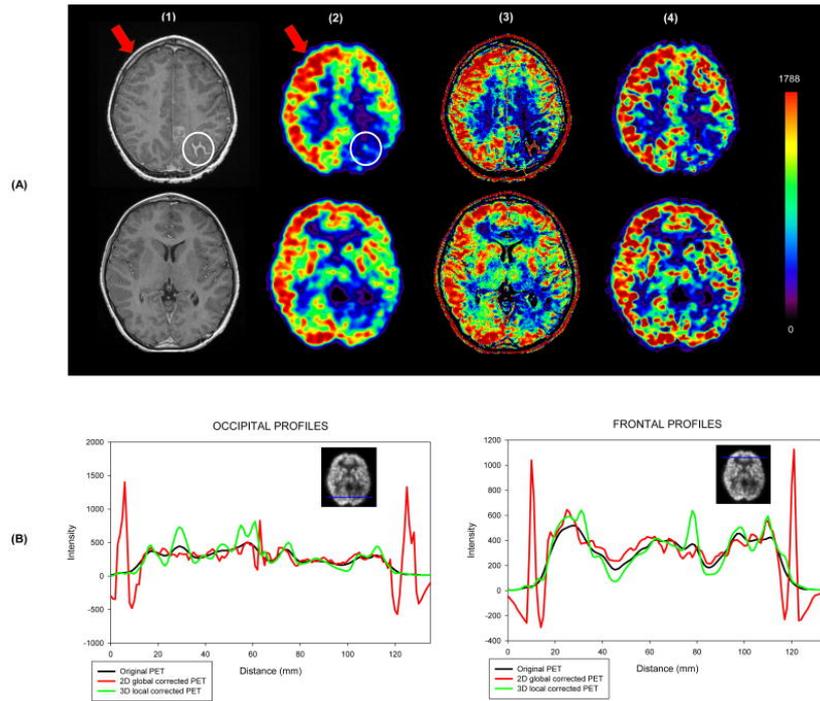

Figure 6

a clinical whole body CT/[18] F-FDG PET study: (1) CT, (2) original non corrected PET, (3) PVE corrected images using the 2D global MMA algorithm, and (4) PVE corrected images using the 3D local MMA approach.
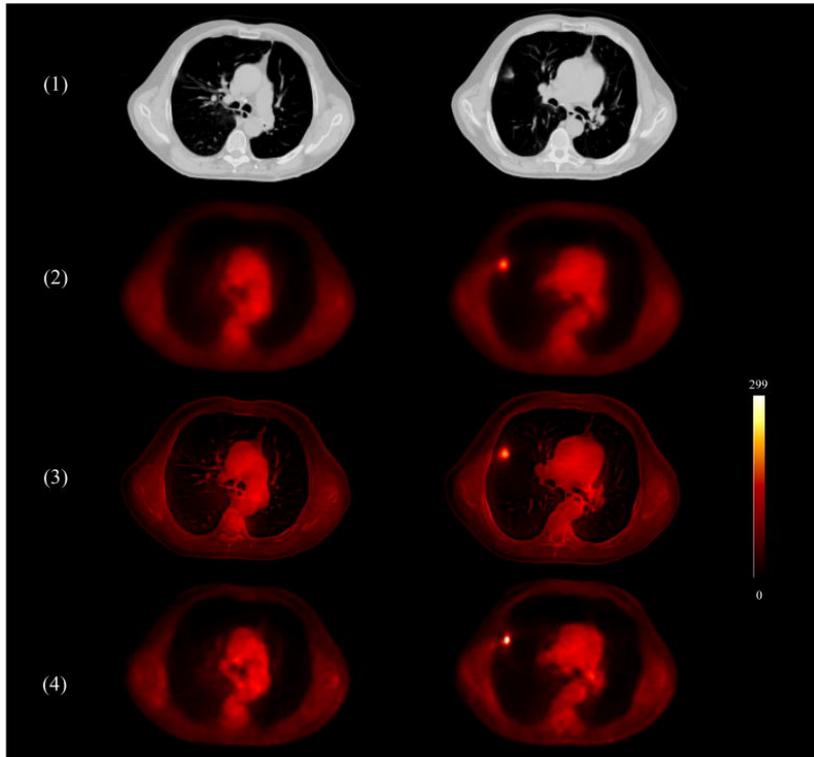
Table 1

FWHM values of the residual scales for an initial FWHM of 1mm and initial voxel sizes of 0.6, 1 and 1.4 mm. The equation formula provided by the software is presented.

	0.60	1.00	1.40	x
Voxel size of the initial image (mm)	0.60	1.00	1.40	x
FWHM residual scale 1 (mm)	1.56	2.61	3.65	2.61 * x
FWHM residual scale 2 (mm)	3.38	5.64	7.90	5.64 * x
FWHM residual scale 3 (mm)	6.89	11.48	16.08	11.48 * x

Table 2

ROI quantification (mean ± SD of the uptake value (kBq/ml) in different ROIs) for the original whole body PET image and the corrected one using the GTM, the 2D global and the 3D local MMA approach. Note that there is no SD in the case of the GTM approach since it is a ROI based PVE correction approach.

Activity (kBq/ml)	ROI lung	ROI lesion	ROI bone
ORIGINAL PET	1.5 ± 0.1	8.9 ± 1.4	5.2 ± 0.5
GTM	1.2	10.9	5.5
2D GLOBAL	1.3 ± 0.3	10.3 ± 1.6	6.7 ± 1.7
3D LOCAL	1.4 ± 0.1	12.8 ± 1.9	5.3 ± 0.6